GEOPHYSICS, VOL. 76, NO. 1 (JANUARY-FEBRUARY 2011); P. SA35–SA49, 14 FIGS., 1 TABLE.
10.1190/1.3521291

Interferometric velocity analysis using physical and nonphysical energy

Simon King[1], Andrew Curtis[1], and Travis L. Poole[2]

ABSTRACT

In controlled-source seismic interferometry, waves from a surrounding boundary of sources recorded at two receivers are crosscorrelated and summed to synthesize the interreceiver Green's function. Deviations of physically realistic source and receiver geometries from those required by theory result in errors in the Green's function estimate. These errors are manifested as apparent energy that could not have propagated between receiver locations — so-called nonphysical energy. We have developed a novel method of velocity analysis that uses both the physical and nonphysical wavefield energy in the crosscorrelated data generated between receiver pairs. This method is used to constrain the root-mean-square (rms) velocity and layer thickness of a locally 1D medium. These estimates are used to compute the piecewise constant interval velocity. Instead of suppressing multiple energy as in conventional common midpoint velocity analysis, the method uses the multiply reflected wavefield to further constrain the rms velocity and layer-thickness estimates. In particular, we determined that the nonphysical energy contains useful physical information. By using the nonphysical energy associated with the truncation of the source boundary and the crosscorrelation of reflected waves, a better-defined estimate of the rms velocity and layer thickness is achieved. Because this energy is excited far from the receiver pair, the technique may be ideally suited to long-offset seismic reflection data. We found that interferometric velocity analysis works best to characterize the first few layers beneath a receiver array. We have considered an acquisition configuration that can be used in a marine seismic setting.

INTRODUCTION

In reflection seismology, we aim to infer quantitative information about the physical properties of the subsurface. In particular, an accurate velocity model is essential to characterize the subsurface geology and in many instances is a prerequisite for imaging or migration. The most common form of velocity analysis in exploration seismology begins with the construction of a velocity spectrum (Taner and Koehler, 1969). Obtained from common midpoint (CMP) gathers, the velocity spectrum displays the signal coherency along hyperbolic traveltimes as a function of the root-mean-square (rms) velocity and the zero-offset two-way traveltime. In general, peaks in the velocity spectrum that have a high moveout velocity are associated with primary reflections. The rms velocities and traveltimes at these peaks are selected and used to perform a normal moveout (NMO) correction that flattens the corresponding traveltime hyperbola. In this process, multiples are treated as noise. They can be distinguished from the primary reflections because they show a lower moveout velocity at the equivalent traveltime of the primary reflections. For this reason, they are often suppressed by NMO correction and subsequent stacking. To derive the interval velocity for each layer, the picked rms velocity and traveltime pairs are input to the Dix equation (Dix, 1955).

This methodology often forms the basis of the current industry practice for obtaining an initial stacked section of the subsurface. However, a disadvantage of this approach is its failure to use information from the multiple arrivals. In fact, multiple energy clutters the velocity spectra, making the picking of primary energy more difficult. Multiples provide secondary ensonification of the subsurface and hence, in principle, provide additional information. For example, Muijs et al. (2007) use free-surface multiples together with the primary arrivals to image subsurface reflectors. Despite this potential advantage, multiples are often removed from or suppressed in data prior to the onset of velocity analysis.

Manuscript received by the Editor 1 March 2010; revised manuscript received 17 August 2010; published online 11 January 2011.
[1]University of Edinburgh, School of GeoSciences, and Edinburgh Collaborative of Subsurface Science and Engineering, Edinburgh, U. K. E-mail: s.j.king@sms.ed.ac.uk; andrew.curtis@ed.ac.uk.
[2]Formerly University of Edinburgh, School of GeoSciences, and Edinburgh Collaborative of Subsurface Science and Engineering, Edinburgh, U. K.; presently University of Edinburgh, Business School, Edinburgh, U. K. E-mail: travis.poole@ed.ac.uk.

Another drawback of conventional velocity analysis is that it does not comply with wide-angle or long-offset seismic reflection data. Specifically, when the small-spread approximation is violated (i.e., the maximum offset is large compared with the depth of the target) the conventional two-term hyperbolic traveltime equation derived by Taner and Koehler (1969) becomes invalid. To overcome this limitation, several alternative techniques have been proposed. The method of Diebold and Stoffa (1981) and Schultz (1982) transforms the seismic reflection data into the τ-p domain. Here, $p = dt/dx$ is the horizontal slowness or ray parameter, and $\tau = t - px$ where t and x are the two-way traveltime and horizontal offset, respectively. Such an approach aids the interpretation of reflection data in horizontally layered media and lends itself well to the direct estimation of interval velocities. González-Serrano and Claerbout (1984) outline a method to obtain the interval velocity using a linear transformation of the CMP gather. Several authors have built upon this work, and each such study aims to obtain the interval velocities and layer thicknesses from wide-angle or long-offset seismic reflection data (Nowroozi, 1990; Sain and Kaila, 1996; Kumar et al., 2003).

In this paper, we propose a new method of interval velocity and layer-thickness estimation closely associated with seismic interferometry. Seismic interferometry refers to a set of techniques where new Green's functions are synthesized between pairs of receiver locations (i.e., we construct seismograms as though one of the receivers had been an impulsive source) by crosscorrelating and summing waves from a surrounding boundary of sources that were recorded at the receivers (Wapenaar, 2004; van Manen et al., 2005, 2006; Wapenaar and Fokkema, 2006; Curtis et al., 2006). Depending on the context of the seismic experiment, the recorded wavefield may be illuminated passively by ambient seismic noise (Campillo and Paul, 2003) or excited by active controlled sources, as in an industrial seismic setting (Bakulin and Calvert, 2006). Not constrained to crosscorrelation, Vasconcelos and Snieder (2008a, 2008b) show that interferometry can be estimated by deconvolution. This approach has been extended by Wapenaar et al. (2008) to multidimensional deconvolution. In deconvolutional interferometry, the emergent Green's function has the advantage of being relatively free from source properties. It has also been shown that the electromagnetic (Slob and Wapenaar, 2007; Slob et al., 2007) and surface wave (Halliday and Curtis, 2008, 2009b) Green's functions in attenuative media can be estimated by crossconvolutional interferometry. In reciprocal geometries (often used in exploration seismics), intersource point Green's functions can also be constructed using recordings on a surrounding array of receivers (Curtis et al., 2009). Snieder et al. (2009) provide a comparison of interferometric techniques.

It is evident that to date, much attention has focused on the estimation of the Green's function and its subsequent improvement to match the desired impulse response between receiver pairs (Douma and Snieder, 2006; Mehta et al., 2007; Wapenaar et al., 2008; van der Neut and Bakulin, 2009; Curtis and Halliday, 2010). However, in many of these examples, where interferometric theory cannot be realized exactly in practice, nonphysical arrivals persist in the Green's function estimate. Nonphysical arrivals still satisfy the wave equation and thus contain information about the nature of the subsurface. They can result from several mechanisms but usually depend upon the acquisition geometry and the scattering and/or physical properties of the medium under consideration. In exploration seismology, sources are predominantly located near the surface of the earth; in this instance, the source boundary is incomplete (e.g., there are no sources in the deep subsurface), and sources positioned near the array end points lead to uncanceled nonphysical contributions (Snieder et al., 2006b). Snieder et al. (2006b) also show that the cross-terms of reflected waves lead to nonphysical arrivals that would otherwise be canceled by the missing boundary sources at depth. Because these nonphysical arrivals are dynamically equivalent to peg-leg multiples, those authors term them spurious multiples. For body waves scattered by a single diffractor, Snieder et al. (2008) derive expressions for the nonphysical arrivals as part of a generalized optical theorem. Halliday and Curtis (2009a) present a similar derivation for surface waves. Mikesell et al. (2009) demonstrate that the crosscorrelation of refracted energy leads to a nonphysical arrival they term the virtual refraction. The gradient of this nonphysical arrival defines the velocity of the underlying medium in a two-layer model.

In this paper, we extract rms velocity and layer-thickness estimates using the theory of controlled-source seismic interferometry. We perform rms velocity and layer-thickness estimation on so-called correlation gathers between receiver pairs (defined below). These estimates are then used to derive the interval velocity. Unlike the standard velocity-estimation techniques described above, we incorporate free-surface and interbed multiples in our analysis to further constrain the rms velocity and layer-thickness estimates. We also use the nonphysical energy contained within the correlation gather. This nonphysical energy is associated with the crosscorrelation of reflected waves by sources positioned near the end points of the source boundary. In particular, we find that by using these sources, we obtain a more coherent estimate of the rms velocity and layer thickness. Furthermore, these sources are located at far offset from the receiver pair. Hence, the method presented is applicable to long-offset seismic reflection records.

We begin by reviewing controlled-source interferometric theory and defining the correlation gather. We then introduce the deconvolution gather and in the following examples explain why the deconvolution gather approximates that of crosscorrelation. Following this, we describe the process of velocity and layer-thickness estimation using a single acoustic layer over a half-space model. Next, the method is extended to find the rms and interval velocities of a multilayered acoustic model. In the subsequent section, we compare the method presented here with standard CMP velocity techniques. Finally, we discuss the implications of this work for exploration seismology.

SEISMIC INTERFEROMETRY

Interferometry by crosscorrelation

In this paper we consider controlled-source interferometry where a set of receivers are illuminated by impulsive active sources. Say two receivers, positioned at $\mathbf{x}_1$ and $\mathbf{x}_2$, record the response from a surrounding boundary of volume-injection rate, monopolar, and dipolar sources in a medium without attenuation (Figure 1). Using Rayleigh's reciprocity theorem and the invariance of the wave equation under time reversal, Wapenaar (2004), van Manen et al. (2005), and Wapenaar and Fokkema (2006) show that the exact acoustic Green's function $\hat{G}(\mathbf{x}_1,\mathbf{x}_2,\omega) + \hat{G}^*(\mathbf{x}_1,\mathbf{x}_2,\omega)$ between the two receivers can be expressed in the frequency domain as

$$\hat{G}(\mathbf{x}_1,\mathbf{x}_2,\omega) + \hat{G}^*(\mathbf{x}_1,\mathbf{x}_2,\omega) = \oint_{\partial S} \frac{-1}{j\omega\rho(\mathbf{x})}((\partial_i \hat{G}(\mathbf{x}_1,\mathbf{x},\omega))\hat{G}^*(\mathbf{x}_2,\mathbf{x},\omega) - \hat{G}(\mathbf{x}_1,\mathbf{x},\omega)\partial_i \hat{G}^*(\mathbf{x}_2,\mathbf{x},\omega))n_i d^2\mathbf{x}, \quad (1)$$

where j is $\sqrt{-1}$, ω is the angular frequency, $\rho(\mathbf{x})$ is the density at $\mathbf{x}$, the asterisk $(*)$ denotes complex conjugation (time reversal in the time domain), and n_i represents the component of the outward pointing normal in the ith direction to the source boundary ∂S. Here, $\hat{G}$ denotes the frequency-domain Green's functions. The Green's function between a monopole source positioned at $\mathbf{x}$ and a receiver located at $\mathbf{x}_r$ is expressed by $\hat{G}(\mathbf{x}_r,\mathbf{x},\omega)$ for $r = 1,2$. The Green's function between a dipole source at $\mathbf{x}$, with the dipole aligned with the coordinate axis i, is expressed by $\partial_i \hat{G}(\mathbf{x}_r,\mathbf{x},\omega)$. Einstein's summation convention applies throughout. To generate the exact Green's function between the receiver pair, it is necessary that the source boundary ∂S completely encloses $\mathbf{x}_1$ and $\mathbf{x}_2$, except for portions of ∂S that coincide with the earth's free surface, at which locations the integrand in equation 1 is equal to zero (van Manen et al., 2005, 2006; Wapenaar and Fokkema, 2006).

To apply seismic interferometry with only monopolar sources (e.g., vibrator trucks, dynamite, and airguns), Wapenaar and Fokkema (2006) assume that the medium is locally smooth around each source, as well as homogeneous outside the boundary ∂S. Furthermore, Wapenaar and Fokkema (2006) assume the far-field approximation and that the energy leaving each source is approximately perpendicular to ∂S. The Green's function $\hat{G}(\mathbf{x}_1,\mathbf{x}_2,\omega)$ and its complex conjugate is then expressed approximately as

$$\hat{G}(\mathbf{x}_1,\mathbf{x}_2,\omega) + \hat{G}^*(\mathbf{x}_1,\mathbf{x}_2,\omega) \approx \oint_{\partial S} \frac{2}{\rho c}\hat{G}(\mathbf{x}_1,\mathbf{x},\omega)\hat{G}^*(\mathbf{x}_2,\mathbf{x},\omega)d^2\mathbf{x}, \quad (2)$$

where ρ and c are the density and velocity at $\mathbf{x}$, respectively, and are assumed to be constant at and outside the boundary. After integrating over source locations ∂S, we obtain an approximation to the monopolar Green's function $\hat{G}(\mathbf{x}_1,\mathbf{x}_2,\omega)$ as though a source was fired at $\mathbf{x}_2$ and a response was received at $\mathbf{x}_1$ (Figure 1). Essentially, the crosscorrelation operation isolates the phase differences between waves recorded at both of the receivers (Snieder, 2004). Thus, the phase of the Green's function estimate should remain equal to that of equation 1; however, if not fulfilled, the approximation introduces an amplitude error.

The Green's function between a boundary source positioned at $\mathbf{x}$ and recorded at $\mathbf{x}_1$ can be decomposed into its direct and reflected component, $\hat{G}_d(\mathbf{x}_1,\mathbf{x},\omega)$ and $\hat{G}_r(\mathbf{x}_1,\mathbf{x},\omega)$, respectively:

$$\hat{G}(\mathbf{x}_1,\mathbf{x},\omega) = \hat{G}_d(\mathbf{x}_1,\mathbf{x},\omega) + \hat{G}_r(\mathbf{x}_1,\mathbf{x},\omega). \quad (3)$$

Substituting equation 3, the Green's function between $\mathbf{x}$ and $\mathbf{x}_1$, and its equivalent for $\mathbf{x}_2$ into the interferometric integral in equation 2, we can express the crosscorrelation as the sum of four terms:

$$\begin{aligned}\hat{G}(\mathbf{x}_1,\mathbf{x}_2,\omega) + \hat{G}^*(\mathbf{x}_1,\mathbf{x}_2,\omega) \approx{}& \frac{2}{\rho c}\underbrace{\oint_{\partial S} \hat{G}_d(\mathbf{x}_1,\mathbf{x},\omega)\hat{G}_d^*(\mathbf{x}_2,\mathbf{x},\omega)d^2\mathbf{x}}_{C_1} \\ &+ \frac{2}{\rho c}\underbrace{\oint_{\partial S} \hat{G}_r(\mathbf{x}_1,\mathbf{x},\omega)\hat{G}_d^*(\mathbf{x}_2,\mathbf{x},\omega)d^2\mathbf{x}}_{C_2} \\ &+ \frac{2}{\rho c}\underbrace{\oint_{\partial S} \hat{G}_d(\mathbf{x}_1,\mathbf{x},\omega)\hat{G}_r^*(\mathbf{x}_2,\mathbf{x},\omega)d^2\mathbf{x}}_{C_3} \\ &+ \frac{2}{\rho c}\underbrace{\oint_{\partial S} \hat{G}_r(\mathbf{x}_1,\mathbf{x},\omega)\hat{G}_r^*(\mathbf{x}_2,\mathbf{x},\omega)d^2\mathbf{x}}_{C_4}. \end{aligned} \quad (4)$$

Term C_1 represents the crosscorrelation of the direct waves at both receivers, C_2 represents the crosscorrelation of the direct wave at $\mathbf{x}_2$ with the reflected waves at $\mathbf{x}_1$, C_3 represents the crosscorrelation of the reflected waves at $\mathbf{x}_2$ with the direct wave at $\mathbf{x}_1$, and C_4 represents the crosscorrelation of the reflected waves at both receivers.

Before integration, it is useful to display the crosscorrelations between the receiver pair in equation 2 as a function of source position $\mathbf{x}$ (van Manen et al., 2005). This data display is referred to as the correlation gather by Mehta et al. (2008). To illustrate this concept, we consider an acoustic model and the acquisition source geometry shown in Figure 2. The acquisition geometry represents a typical configuration of sources and receivers that could be extracted from marine seismic data. The data set, consisting of 400 shot gathers each with 301 receivers, was modeled using a 2D finite-difference scheme with a perfectly reflecting upper free surface (Robertsson et al., 1994). Each receiver records the response from a pressure source

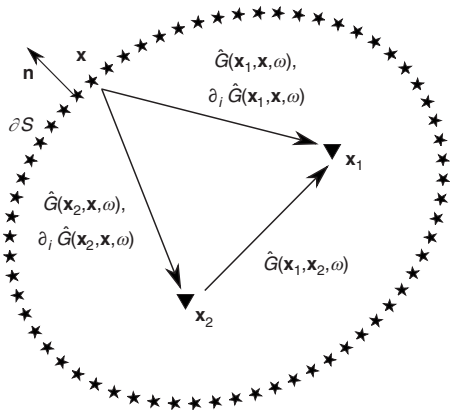

Figure 1. Two receivers, positioned at $\mathbf{x}_1$ and $\mathbf{x}_2$ (denoted by triangles), record the wavefield from sources (denoted by stars) that are fired sequentially at $\mathbf{x}$ on the source boundary ∂S. The frequency-domain Green's function from a monopolar source at $\mathbf{x}$ and received at $\mathbf{x}_1$ is denoted by $\hat{G}(\mathbf{x}_1,\mathbf{x},\omega)$. The frequency-domain Green's function from a dipolar source at $\mathbf{x}$ and received at $\mathbf{x}_1$ is denoted by $\partial_i \hat{G}(\mathbf{x}_1,\mathbf{x},\omega)$. The same definitions apply for the Green's functions recorded at $\mathbf{x}_2$.

at a sample rate of 4 ms for a total of 3 s. Note that the source boundary, as defined by seismic interferometry in equations 1 and 2, is incomplete in Figure 2 (side and lower boundary source sections are missing). Therefore, we would expect any subsequent Green's function estimates made using this data set to contain both physical and nonphysical arrivals.

For $\mathbf{x}_1$ and $\mathbf{x}_2$ in equation 2, we choose receivers 151 and 1, respectively, offset from each other by 600 m. Figure 3a shows the correlation gather, Figure 3b displays the Green's function estimate, and Figure 3f shows the true Green's function between these receiver locations. To create the correlation gather, we have crosscorrelated the full wavefield (i.e., the direct, primary, and free-surface multiples) at receiver 1 with the full wavefield at receiver 151 and plotted the result in the time domain as a function of the source position.

Any significant energy in the correlation gather occurs at the traveltime *differences* between waves recorded at the two receivers. Using the method of images (Brekhovskikh, 1960), we can show that these traveltime difference curves assume the form

$$\delta \mathbf{t} = \frac{\sqrt{x_j^2 + (2b_j D_1 \pm z_s \pm z_j)^2}}{v_1} - \frac{\sqrt{x_i^2 + (2b_i D_1 \pm z_s \pm z_i)^2}}{v_1}, \tag{5}$$

where $\delta \mathbf{t}$ is the traveltime difference; x_i and x_j are the horizontal distances from each source to receiver r_i and r_j, respectively; $b_i(b_j)$ is the number of bounce points from the bottom reflecting interface to receiver $r_i(r_j)$, and the receivers are at depth $z_i(z_j)$; D_1 is the depth of the interface; z_s is the depth of the source; and v_1 is the P-wave interval velocity of the medium (Figure 2). The sign of z_s is negative when waves are downgoing from the source and positive when waves are upgoing. The sign of $z_i(z_j)$ is negative when waves are upgoing at the receiver and positive when waves are downgoing. In the examples that follow, we set $i = 1$ and $j = 151$.

We now interpret the traveltime curves in the correlation gather using equation 5. For this, we assume that $D_1 = 150$ m, $v_1 = 1500$ m/s, and the reflected wavefields are downgoing at the source and upgoing at the receiver (i.e., the sign of z_s and $z_i(z_j)$ is negative).

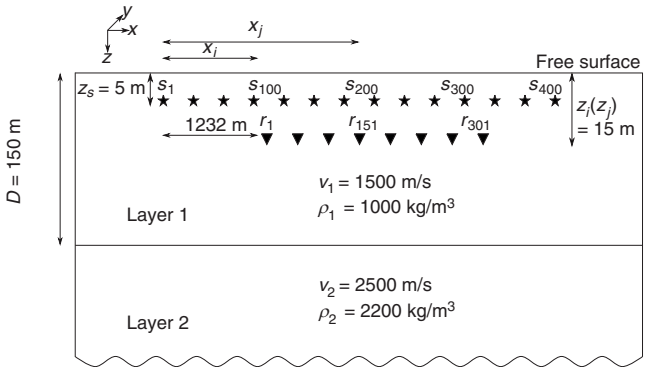

Figure 2. Model consisted of a layer over a half-space, both homogeneous. Layer 1 is bounded on top by a free surface and below by a planar interface at a depth of 150 m. The velocities (v_1 and v_2) and densities (ρ_1 and ρ_2) are shown. Four hundred sources ($s_1,\ldots,s_{400}$) indicated by stars illuminated 301 receivers ($r_1,\ldots,r_{301}$), indicated by triangles. Sources are fixed at a 5-m depth and separated by 8-m intervals, whereas receivers are positioned at a 15-m depth and separated by 4-m intervals. Note that for clarity we do not show every source and receiver.

The traveltime, which is composed of linear segments and which intersects the time axis at ± 0.4 s in Figure 4a, highlights the energy in the direct arrival at r_{151} crosscorrelated with the direct arrival at r_1, term C_1 in equation 4. Working downward in Figure 4a, the next curve illustrates the traveltime for energy in the primary reflection at r_{151} crosscorrelated with the direct arrival at r_1. The following curve displays the traveltime for energy in the first-order multiple at r_{151} crosscorrelated with the direct arrival at r_1 and so on (the remaining curves are defined in the caption to Figure 4a). These curves are all associated with the term C_2 in equation 4. By contrast, we now calculate the traveltime curves by fixing the direct arrival at r_{151} and varying the number of bounce points to r_1. These traveltime curves are displayed in Figure 4b and are associated with the term C_3 in equation 4. Finally, we consider traveltime curves associated with term C_4. Figure 4c shows traveltime curves of reflected waves that have the same number of bounce points to each receiver. These curves have similar traveltime differences and hence are positioned closely together. Figure 4d displays the traveltime curves of reflected waves that have a differing number of bounce points to each receiver.

The V-shaped traveltime curves, associated with terms C_2 and C_3, correspond to the causal and acausal reflections, respectively (Snieder et al., 2006b). The extrema of these curves (indicated by the boxes in Figure 3a) are termed stationary-phase points because the wave phase becomes stationary with respect to the boundary source location. Several authors have analyzed the contribution of stationary-phase points to interferometric integrands such as in equations 1 and 2 (Snieder, 2004; Sabra et al., 2005; Halliday and Curtis, 2008, 2009b). In the summation over sources (integration), if the amplitude of the energy does not vary rapidly with source position then energy around these stationary-phase points sums constructively, whereas other energy sums destructively. Stationary energy thus provides the dominant contribution to the estimate of the true homogeneous Green's function on the left-hand side of equation 2. Consistently with previous studies, we therefore refer to the energy around these points (i.e., approximately between sources 150 and 160) as physical energy. Note that we also obtain stationary-phase points, associated with term C_4, that cluster to the left of the V-shaped traveltime curves (Figure 4d). Energy to the left of these latter stationary-phase points is nonstationary and is therefore nonphysical. The energy in this so-called nonstationary region will lead to nonphysical endpoint contributions (Snieder et al., 2006b). In the velocity analysis procedure outlined in the next section, we will show that the nonphysical contribution from low-order multiples associated with term C_4 between sources 1 and 80,

$$\hat{G}_{np}(\mathbf{x}_1,\mathbf{x}_2,\omega) + \hat{G}^*_{np}(\mathbf{x}_1,\mathbf{x}_2,\omega) \approx \frac{2}{\rho c}\underbrace{\int_1^{80} \hat{G}_r(\mathbf{x}_1,\mathbf{x},\omega)\hat{G}^*_r(\mathbf{x}_2,\mathbf{x},\omega)d^2\mathbf{x}}_{C_4}, \tag{6}$$

can constrain the rms velocity and layer thickness.

Interferometry by deconvolution

In certain situations, deconvolutional interferometry seems a more natural operation than crosscorrelational interferometry because it removes much of the signature of nonimpulsive boundary sources, leaving a relatively impulsive source signal in the Green's function estimate (Vasconcelos and Snieder, 2008b). Snieder et al.

(2006a) show how deconvolution interferometry can be used to obtain the building response at different floors of a multistory structure compliant for different boundary conditions. Vasconcelos and Snieder (2008a) further develop the theory of deconvolution interferometry and outline an application related to seismic-while-drilling and imaging of the San Andreas fault in California, U. S. A. (Vasconcelos and Snieder, 2008b).

With reference to Figure 1, deconvolutional interferometry for a one-dimensional medium is defined as follows:

$$\hat{D}(\mathbf{x}_1,\mathbf{x}_2,\omega) = \oint_{\partial S} \frac{\hat{G}(\mathbf{x}_1,\mathbf{x},\omega)\hat{G}^*(\mathbf{x}_2,\mathbf{x},\omega)d^2\mathbf{x}}{|\hat{G}(\mathbf{x}_2,\mathbf{x},\omega)|^2 + \varepsilon} \qquad (7)$$

where ε is a stabilization factor associated with the water-level deconvolution approach of Clayton and Wiggins (1976). Vasconcelos and Snieder (2008a) show that when $|G_d|^2 \gg |G_r|^2$ (i.e., the power spectrum of the direct arrival is much greater than the power spectrum of the reflected wavefield), equation 7 reduces to three terms, D_1, D_2, and D_3. The terms D_1 and D_2 are analogous to C_1 and C_2 in crosscorrelational interferometry. The term D_3 is associated with nonphysical arrivals that Vasconcelos and Snieder (2008a) term free-point scattered waves. The obvious difference between equations 2 and 7 is that in equation 7, we divide the numerator by the power spectrum of the Green's function at $\mathbf{x}_2$. Thus, any appreciable source wavelet (that would be convolved with the Green's functions on both sides of equation 2) is removed in equation 7 by division in the frequency domain. If the factor ε is too large, equation 7 simply approximates scaled crosscorrelation interferometry. Conversely, the deconvolution will become unstable if ε is too small. Hence, in deconvolutional interferometry, there exists a trade-off between stabilization and resolution determined by the factor ε, a trade-off that is not present in crosscorrelation interferometry.

We define a second interferometric gather, the deconvolution gather, as the set of integrands contributing to the integral of equation 7 between a fixed receiver pair (i.e., at $\mathbf{x}_1$ and $\mathbf{x}_2$) as a function of source position $\mathbf{x}$. Figure 3c shows the deconvolution gather for receivers 1 and 151, and Figure 3d displays the Green's function estimate. In this instance, the deconvolution gather seems comparable to the correlation gather. However, there is one important difference, indicated by the arrow in Figure 3c. In this region, between source numbers 152 and 156, the requirement that $|G_d|^2 \gg |G_r|^2$ holds, and we achieve causal reflected waves, i.e., term D_2, as expected by the theory (Vasconcelos and Snieder, 2008a). Figure 3e shows a close-up of this region. As a point of note, these sources are positioned at the stationary-phase points for causal reflected waves. Outside this region, however, the source ghost (i.e., the wavefield that travels from the source into the subsurface via a single reflection at the free surface) significantly reduces the amplitude of the direct arrival. Hence, the requirement that $|G_d|^2 \gg |G_r|^2$ is no longer valid. This results in causal and acausal contributions that have a phase similar to that of the arrivals in the correlation gather. For this reason, we limit our presentation of the velocity analysis procedure, described in the next section, to the correlation gathers only. However, tests show that the method works just as well for deconvolution gathers.

INTERFEROMETRIC VELOCITY ANALYSIS

For field data, we know the source-receiver geometry and treat both D_1 and v_1 as unknown. For different values of D_1, v_1, b_i, and b_j, we calculate the traveltime difference curves using equation 5 and then measure the signal coherency along each curve in the correlation gather. The aim of interferometric velocity analysis is to find a velocity and layer-thickness estimate that gives the highest coherency of signal along the specified traveltime difference curves. In the following examples, we compute equation 5 by assuming that wave-

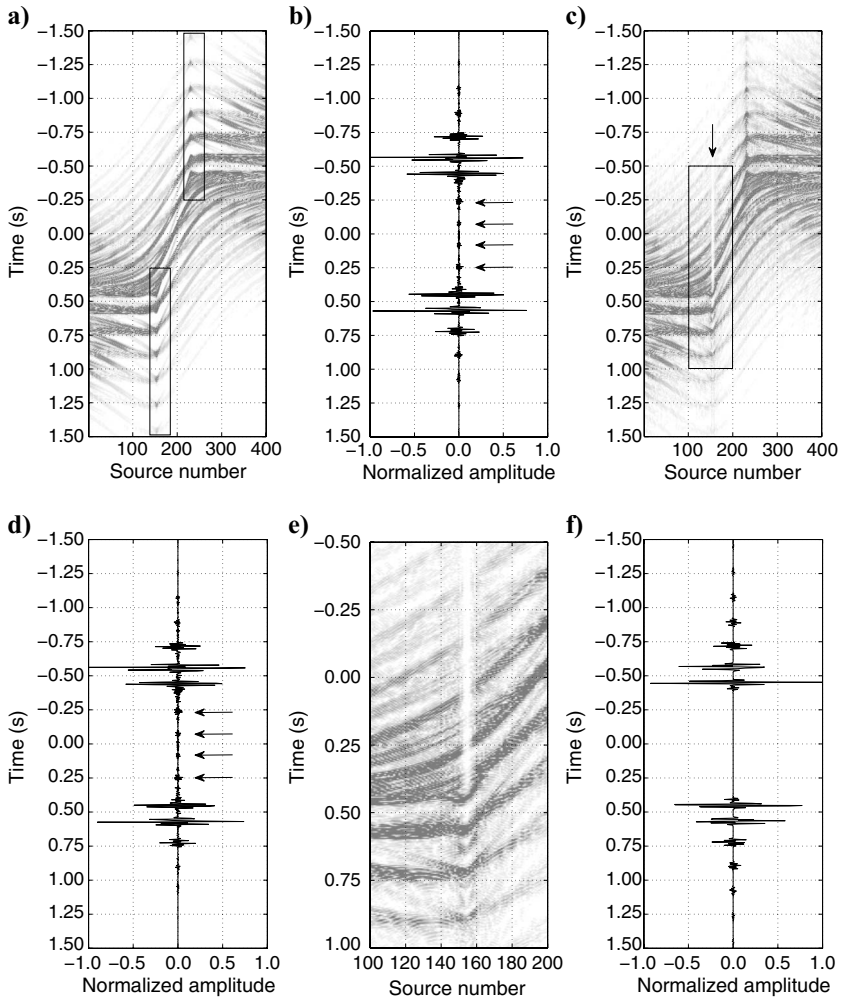

Figure 3. Interferometric estimates and true Green's function for the single layer over half-space model in Figure 2. (a) Correlation gather for receivers 1 and 151 showing arrivals between −1.5 s and 1.5 s. (b) Green's function estimate after summation over source position in (a). (c) Deconvolution gather for receivers 1 and 151. (d) Green's function after summation over source position in (c). In (b) and (d), arrows denote nonphysical arrivals. (e) Close-up of the deconvolution gather showing arrivals within the box in (c). (f) True Green's function plus its time-reversed component.

fields are downgoing at the source and upgoing at the receivers (we do not explicitly decompose the measured wavefield into its upgoing and downgoing components, but this could be done). As a coherency measure, we use a modified version of semblance S_c (Neidell and Taner, 1971), which is defined as the normalized output (E^{out}) to input (E^{in}) energy,

$$S_c = \frac{1}{(b_1 \cdot b_{151})} \sum_{i=1}^{b_1} \sum_{j=1}^{b_{151}} \frac{E_{i,j}^{\text{out}}}{N \cdot E_{i,j}^{\text{in}}} \quad 0 \le S_c \le 1, \tag{8}$$

where N is the number of sources or "traces" in the correlation gather, and the output energy E_{out} and input energy E_{in} are defined as

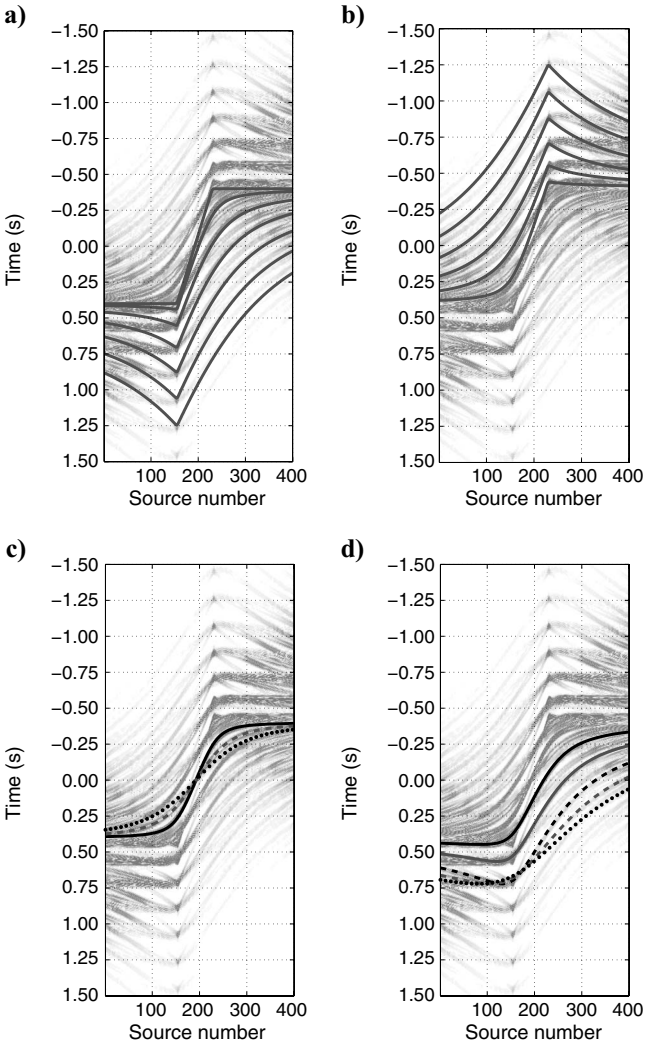

Figure 4. Traveltime curves, calculated using equation 5, plotted on the correlation gather. D, direct arrival; P, primary arrival; M1, first-order multiple (M2, M3, M4, M5, M6, and so on). Crosscorrelations are expressed as DD, where the first letter refers to the direct arrival at r_{151} and the second letter refers to the direct arrival at r_1. Likewise, PD indicates crosscorrelation of the primary arrival at r_{151} and with the direct arrival at r_1. (a) Working downward, the traveltimes are as follows, DD, PD, M1D, M2D, M3D, M4D, and M5D. (b) Working upward, the traveltimes are as follows, DP, DM1, DM2, DM3, DM4, and DM5. (c) Solid black: PP. Dashed gray: M1M1. Dotted black: M2M2. (d) Solid black: M1P. Solid gray: M2P. Dashed black: M3P. Dashed gray: M4M1. Dotted black: M5M2.

$$E_{i,j}^{\text{out}} = \sum_{t(k)=\delta\mathbf{t}-t/2}^{\delta\mathbf{t}+t/2} \left\{ \sum_{\ell=1}^{N} f_{i,j,\ell,t(k)} \right\}^2 \tag{9}$$

and

$$E_{i,j}^{\text{in}} = \sum_{t(k)=\delta\mathbf{t}-t/2}^{\delta\mathbf{t}+t/2} \sum_{\ell=1}^{N} f_{i,j,\ell,t(k)}^2, \tag{10}$$

where f is a function of D_1, v_1, b_1, and b_{151} and is the amplitude value at the ℓth source at time $\delta\mathbf{t}$ within a time window $[-t/2\ \ t/2]$. After summation over the number of bounce points and number of sources, we obtain a 2D spectrum in velocity and layer thickness. Note that in equations 8–10, we consider only wavefields with $b_i(b_j) \ge 1$, and hence, the traveltime difference curves correspond to term C_4 in equation 4.

We first consider the velocity-layer-thickness spectra computed using all 400 sources in equations 8–10. Figure 5a shows the velocity-layer-thickness spectrum computed using energy up to the first-order multiple ($b = 2$) in the correlation gather, and Figure 5b dis-

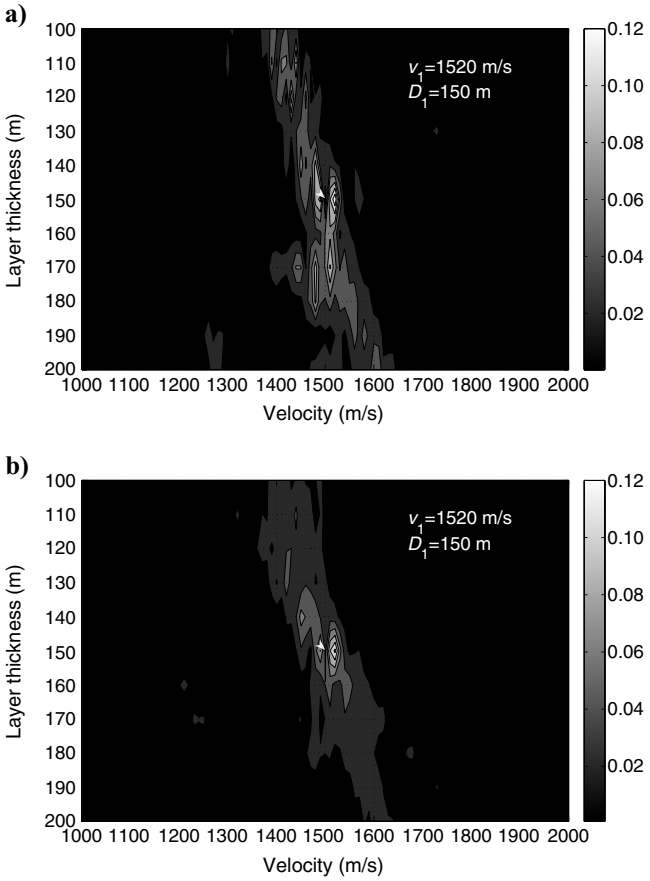

Figure 5. Spectra computed from the correlation gather in Figure 3a. The velocity v_1 spans from 1000 to 2000 m/s and increments every 10 m/s. The layer thickness D_1 spans from 100 to 200 m and increments every 10 m. We use a time window of 10 ms. In each of the following spectra we indicate the true value of velocity and layer thickness with an arrowhead and display the velocity-thickness pair with the highest signal coherency in the upper right-hand corner. (a) Semblance computed using all 400 sources and energy up to the first-order multiple ($b = 2$). (b) As for (a) but computed using energy up to the third-order multiple ($b = 4$).

plays the same plot computed up to the third-order multiple ($b = 4$). It is clear that by increasing the order of multiples in the semblance computation, Figure 5b clarifies which is the single, correct peak, which lies close to the true value of velocity and layer thickness.

We now consider using only the first 80 sources in equations 8–10 (contributing nonphysical energy to the interferometric integrand in equation 2). For a typical marine survey, this represents the data geometries commonly recorded. In Figure 6a and b, we display the velocity-layer-thickness spectra for energy up to the first-order multiple ($b = 2$) and third-order multiple ($b = 4$), respectively. By incorporating a higher number of multiples in Figure 6b, we achieve a more accurate estimate of velocity and layer thickness.

At first glance, the spectra in Figures 5 and 6 appear very similar. However, careful attention should be turned toward the coherency values (scale bars) in both figures. The maximum coherency value in Figure 6, using only 80 sources, is more than three times as large as the maximum coherency value of the respective semblance when all 400 sources are considered, in Figure 5. This implies that by using fewer sources, positioned at the end points of the source boundary, which largely contribute to nonphysical interferometric arrivals, we achieve a better-defined velocity and layer-thickness estimate. This result appears nonintuitive; however, it may arise because for multiples, the interferometric wavefield diverges for sources positioned in the nonstationary region (see Figure 4d). Thus, the contribution from these arrivals may be emphasized when only these sources are considered in the semblance computation. Moreover, note that the first 80 sources are positioned at far offset from both receivers, and hence, the method works for long-offset seismic reflection data. Thus, we have shown our method, unlike many interferometric imaging applications (e.g., Schuster et al., 2004) that require wavefields to be excited at stationary-phase locations, to be accurate for sources positioned in the nonstationary (i.e., nonphysical) region and also at long offset.

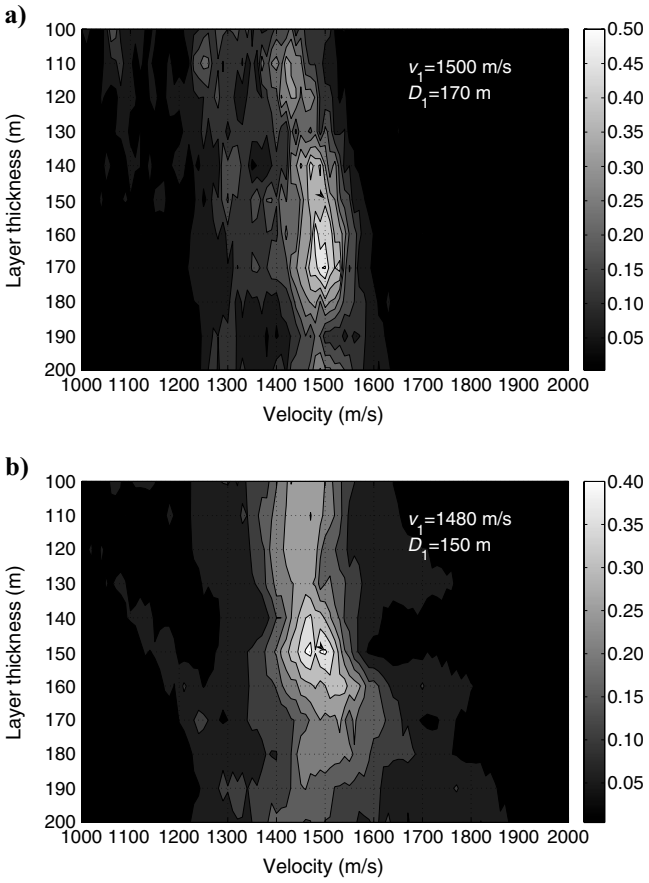

Figure 6. Spectra computed using the nonphysical energy from the correlation gather in Figure 3a. We use the same parameters for v_1, D_1, and t (time window) as in Figure 5. (a) Semblance computed using the first 80 sources and energy up to the first-order multiple ($b = 2$). (b) As for (a) but computed using energy up to the third-order multiple ($b = 4$).

Multilayered model

We now describe interferometric velocity analysis in a multilayered earth. Figure 7 shows a sketch of the multilayered model and acquisition geometry. Each receiver now records the monopolar response for a total of 3.5 s at sample rate of 4 ms. Because we are primarily interested only in reflected waves (i.e., $b_i(b_j) \geq 1$ in equations 8–10), we model the direct arrival in a homogeneous medium (with the velocity and density of layer 1) and subtract the result from each common shot gather prior to performing interferometry by crosscorrelation. Hence, terms such as C_1, C_2, and C_3 in equation 4 are not present in any subsequent crosscorrelational interferometric estimate. This step was not necessary in the single-layer model described in the previous section but may be advisable when more complex models such as this one are considered. Figure 8a shows the correlation gather, Figure 8b displays the corresponding Green's function estimate, and Figure 8c shows the true Green's function.

It is immediately clear that the correlation gather is more complicated than that in Figure 3a. As any significant energy is produced at the traveltime differences between waves recorded at the receiver

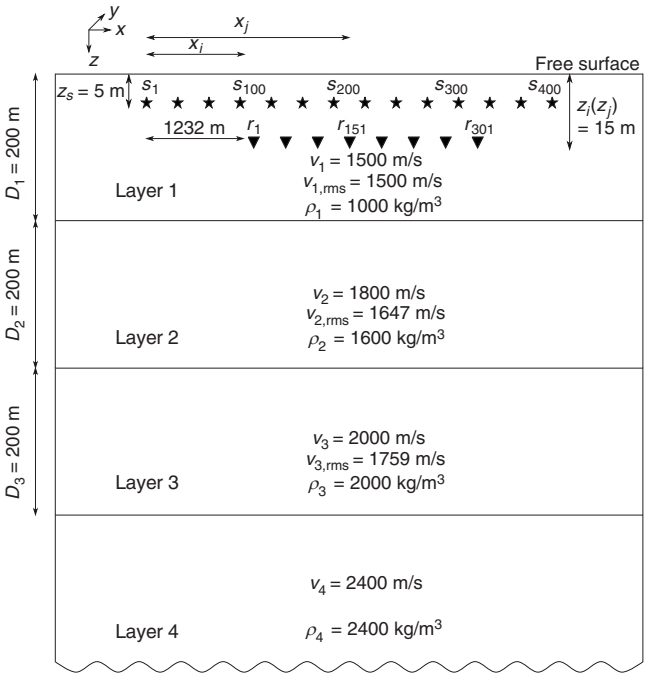

Figure 7. Model consisting of four homogeneous layers separated by three interfaces positioned at 200-m intervals. The interval velocities ($v_1,\ldots,v_4$), rms velocities ($v_{1,\mathrm{rms}},\ldots,v_{3,\mathrm{rms}}$), and densities ($\rho_1,\ldots,\rho_4$) are shown. The acquisition geometry is the same as in Figure 2.

pair, energy from deeper layers may arrive at the same time as energy from shallow layers and therefore mask that energy. This makes an interpretation of arrivals such as those depicted in Figure 4 more difficult in the multilayer case. Nevertheless, we can still identify similar features, such as the stationary-phase and nonstationary regions.

When we have a sequence of layers, we adopt a "layer-stripping" approach. As we now consider a multilayered model, any velocity estimate will be the rms velocity. We determine the rms velocity and thickness of each layer in turn, beginning at the surface and progressing with depth. In the final step, these estimates are converted to interval velocities. Let us first consider $v_{1,\mathrm{rms}}$ and D_1 of layer 1. The traveltime moveout formula due to the interference of wavefields in layer 1 is expressed in equation 5. We adopt the same approach to calculate semblance as described in the previous section, for the time being ignoring energy in the gather from the interference of wavefields from layers 2 and 3.

Figure 9a displays the rms velocity-layer 1 thickness spectrum calculated using all 400 sources in the correlation gather, and Figure 9b shows the corresponding spectrum calculated using only the first 80 sources. To reduce the impact of arrivals from deeper layers, we consider only multiples up to first order ($b_i = b_j = 2$). In Figure 9a, we achieve four peaks positioned close to the correct values of velocity and layer thickness. However, by considering fewer sources, those that contribute nonphysical energy, we obtain a single peak with a higher coherency estimate than when all sources are included (note the scale bar in Figure 9a and b).

We now investigate the velocity $v_{2,\mathrm{rms}}$ and layer thickness D_2 of layer 2 (Figure 7). We assume that the dominant wavefield contributions in interferometry will occur when the high amplitude free-surface reflections from layer 1 are crosscorrelated with reflections from layer 2. These arrivals are termed spurious multiples by Snieder et al. (2006b) and would vanish at the stationary-phase point given a source boundary below the reflectors. Hence, we assume that significant energy in Figure 8a will have an arrival time equal to

$$\delta \mathbf{t} = T_2^{k,\ell} - T_1^m, \tag{11}$$

where $T_2^{k,\ell}$ is the arrival time of a reflection with k bounces in layer 1 and ℓ bounces in layer 2 and T_1^m is the arrival time of a reflection with m bounces from layer 1. The important aspect of the moveout formula in equation 11 is the fact that we have an estimate of the parameters of T_1^m (i.e., we have found $v_{1,\mathrm{rms}}$ and D_1, as displayed in Figure 9). Hence, the moveout formula varies with respect to the first term $T_2^{k,\ell}$, which depends on the unknowns $v_{2,\mathrm{rms}}$ and D_2.

In Appendix A, we derive the traveltime equation for multiple raypaths in a multilayered model and show that the traveltime $T_2^{k,\ell}$ assumes the form

$$t = t_{0_{\mathrm{mult}}}\left(1 - \frac{1}{S}\right) + \sqrt{\left(\frac{t_{0_{\mathrm{mult}}}}{S}\right)^2 + \frac{x_j^2}{S v_{\mathrm{rms}}^2}} \tag{12}$$

where $t_{0_{\mathrm{mult}}} = 2\Sigma_{k=1}^{M} b_{k,j} D_k / v_k$, $b_{k,j}$ is the number of bounce points in the kth layer to the jth receiver, D_k is the layer thickness, v_k is the interval velocity, M is the number of layers, and S is a constant sometimes referred to as the inhomogeneity factor. Equation 12 is accurate for long-offset seismic reflection data. Substituting the traveltimes in equations 5 and 12 into the traveltime difference formula in equation 11, we obtain

$$\delta \mathbf{t} = \underbrace{t_{0_{\mathrm{mult}}}\left(1 - \frac{1}{S}\right) + \sqrt{\left(\frac{t_{0_{\mathrm{mult}}}}{S}\right)^2 + \frac{x_j^2}{S v_{\mathrm{rms}}^2}}}_{T_2} - \underbrace{\frac{\sqrt{x_i^2 + (2 b_i D_1 \pm z_s \pm z_i)^2}}{v_{1,\mathrm{rms}}}}_{T_1}. \tag{13}$$

We take $M = 2$ (the total number of layers in term T_2). Similar to what is described in the previous section, for different values of b_i in T_1, $b_{k,j}$ in T_2, and different estimates of $v_{2,\mathrm{rms}}$ and D_2, we compute the traveltime difference curves as defined by equation 13. For each curve, we find the signal coherency in the correlation gather. As we consider another set of raypaths in layer 2 (determined by $b_{2,151}$), we redefine semblance as

$$S_c = \frac{1}{(b_1 \cdot b_{1,151} \cdot b_{2,151})} \times \sum_{i=1}^{b_1} \sum_{j=1}^{b_{1,151}} \sum_{m=1}^{b_{2,151}} \frac{E_{i,j,m}^{\mathrm{out}}}{N \cdot E_{i,j,m}^{\mathrm{in}}}$$

$$0 \le S_c \le 1, \tag{14}$$

where

$$E_{i,j,m}^{\mathrm{out}} = \sum_{t(k)=\delta \mathbf{t} - t/2}^{\delta \mathbf{t} + t/2} \left\{ \sum_{\ell=1}^{N} f_{i,j,m,\ell,t(k)} \right\}^2 \tag{15}$$

and

$$E_{i,j,m}^{\mathrm{in}} = \sum_{t(k)=\delta \mathbf{t} - t/2}^{\delta \mathbf{t} + t/2} \sum_{\ell=1}^{N} f_{i,j,m,\ell,t(k)}^2. \tag{16}$$

We take $v_{1,\mathrm{rms}} = 1510$ m/s and $D_1 = 210$ m

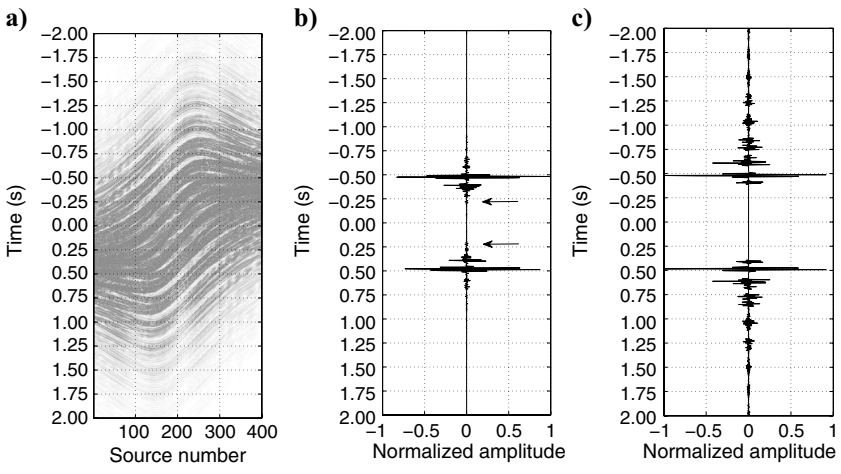

Figure 8. Interferometric estimates and true Green's function for the multilayered model in Figure 7. (a) Correlation gather for receivers 1 and 151 showing arrivals between −2 s and 2 s. (b) Green's function estimate after summation over source position in (a). Arrows denote nonphysical arrivals. (c) True Green's function plus its time-reversed component.

because these values correspond to a single peak with maximum coherency in Figure 9b. Figure 10a displays the rms velocity-layer 2 thickness spectrum computed using all 400 sources and for $b_i = b_{k,j} = 2$ in each layer to each receiver, and Figure 10b displays the corresponding spectrum computed using the first 80 sources (i.e., only the nonphysical energy). By using all sources, we achieve a prominent peak at the correct rms velocity and thickness of layer 2. By using purely the nonphysical energy, we achieve a less well-constrained but more coherent estimate of the subsurface parameters.

Finally, we consider the velocity $v_{3,\mathrm{rms}}$ and layer thickness D_3 of layer 3. As before, we assume that the dominant contributions will occur when free-surface reflections from layer 1 are crosscorrelated with reflections from layer 3. We now take the number of layers $M = 3$ in equation 13. We assume the same values for $v_{1,\mathrm{rms}}$ and D_1 as before but now take $v_{2,\mathrm{rms}} = 1660$ m/s and $D_2 = 200$ m, the average values of the two prominent peaks in Figure 10. We redefine semblance as

$$S_c = \frac{1}{(b_1 \cdot b_{1,151} \cdot b_{2,151} \cdot b_{3,151})} \sum_{i=1}^{b_1} \sum_{j=1}^{b_{1,151}} \sum_{m=1}^{b_{2,151}} \sum_{n=1}^{b_{3,151}} \frac{E^{\mathrm{out}}_{i,j,m,n}}{N \cdot E^{\mathrm{in}}_{i,j,m,n}}$$

$$0 \le S_c \le 1, \tag{17}$$

where

$$E^{out}_{i,j,m,n} = \sum_{t(k)=\delta\mathbf{t}-t/2}^{\delta\mathbf{t}+t/2} \left\{ \sum_{\ell=1}^{N} f_{i,j,m,n,\ell,t(k)} \right\}^2 \tag{18}$$

and

$$E^{in}_{i,j,m,n} = \sum_{t(k)=\delta\mathbf{t}-t/2}^{\delta\mathbf{t}+t/2} \sum_{\ell=1}^{N} f^2_{i,j,m,n,\ell,t(k)}. \tag{19}$$

Figure 11a displays the rms velocity-layer 3 thickness spectrum for all 400 sources and for $b_i = b_{k,j} = 2$ in each layer to each receiver. Figure 11b displays the corresponding spectrum for the first 80 sources (i.e., the nonphysical energy). We find that by using purely the nonphysical energy, we obtain two prominent and highly coherent peaks compared with the case when all 400 sources are considered.

Table 1 provides a summary of the selected rms velocities v_{rms} and layer thicknesses D. We convert these estimates to interval velocity using a formula similar to the Dix equation (Dix, 1955),

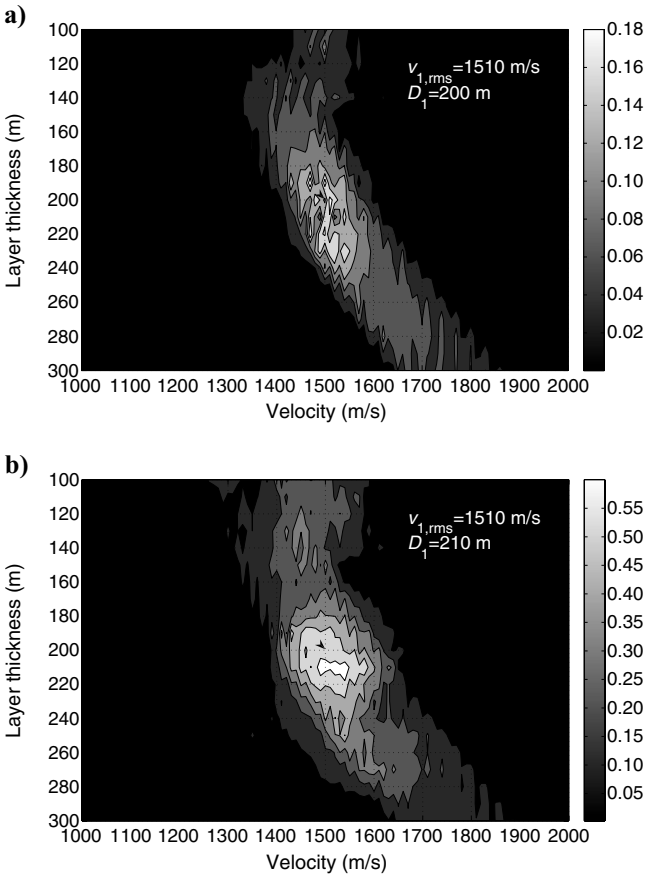

Figure 9. Spectra showing $v_{1,\mathrm{rms}}$ against D_1. The velocity $v_{1,\mathrm{rms}}$ spans from 1000 to 2000 m/s and increments every 10 m/s. The layer thickness D_1 spans from 100 to 300 m and increments every 10 m. We use a time window of 20 ms. (a) Semblance computed from the correlation gather (Figure 8a) using all 400 sources and energy up to the first-order multiple. (b) As for (a) but using only the first 80 sources.

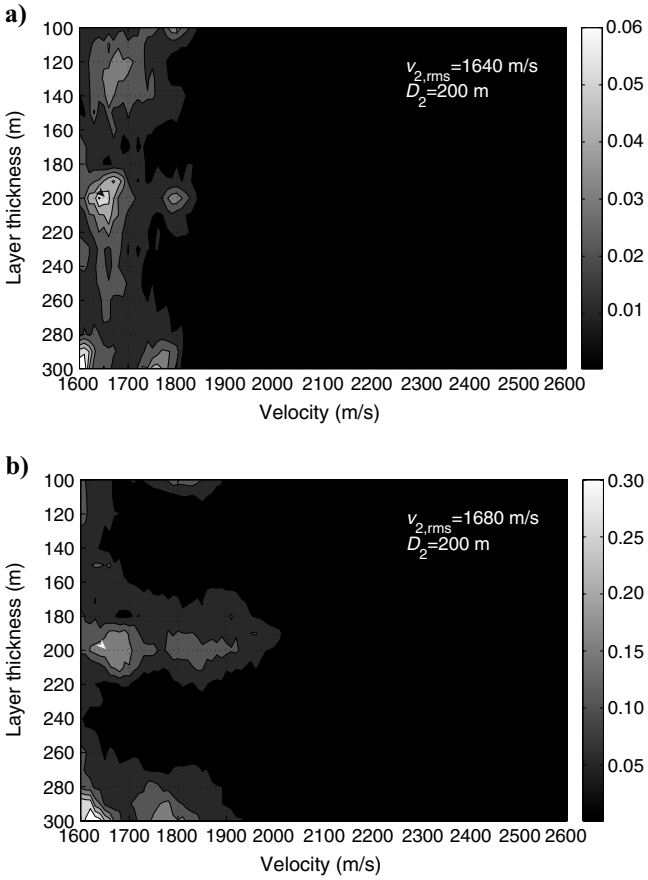

Figure 10. Spectra showing $v_{2,\mathrm{rms}}$ against D_2. We assume that velocity increases with depth, and hence, we choose $v_{2,\mathrm{rms}}$ to vary from 1600 to 2600 m/s and increments every 10 m/s. The layer thickness D_2 spans from 100 to 300 m and increments every 10 m. We use a time window of 20 ms. (a) Semblance computed using all 400 sources in the correlation gather and for $b_i = b_{k,j} = 2$ in each layer. (b) As for as (a) but using only the first 80 sources.

$$v_k = \sqrt{\frac{v_{k,\mathrm{rms}}^2 Z_k - v_{k-1,\mathrm{rms}}^2 Z_{k-1}}{Z_k - Z_{k-1}}}, \tag{20}$$

where v_k is the interval velocity, and Z_k is the depth from the free surface to the kth layer. In this form, equation 20 may be sensitive to inaccurate rms velocities. However, methods exist, such as that outlined by Koren and Ravve (2006), that constrain the inversion in the least-squares sense. It should be noted that in equation 20, and in our analysis so far, we use depths and not two-way traveltimes as expected by the classical Dix formula (Dix, 1955). Given an arbitrary velocity variation, consider the result when we average the rms velocity in time (Appendix A):

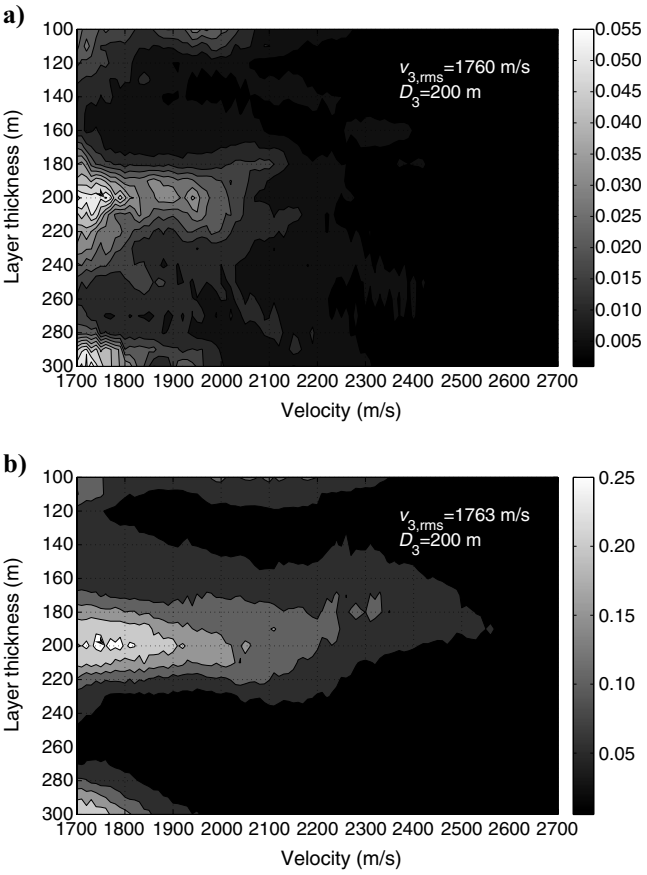

Figure 11. Spectra showing $v_{3,\mathrm{rms}}$ against D_3. The velocity $v_{3,\mathrm{rms}}$ spans from 1700 to 2700 m/s and increments every 10 m/s. The layer thickness D_3 spans from 100 to 300 m and increments every 10 m. We use a time window of 20 ms. (a) Semblance computed using all 400 sources in the correlation gather and for $b_i = b_{k,j} = 2$ in each layer. (b) As for (a) but using only the first 80 sources.

$$v_{\mathrm{rms}}^2(t) = \frac{1}{t}\int_0^t v^2(t)dt = \mu_2. \tag{21}$$

Now consider the result when we average with respect to depth:

$$v_{\mathrm{rms}}^2(z) = \frac{1}{z}\int_0^z v^2(z)dz = \frac{\displaystyle\int_0^t v^3(t)dt}{\displaystyle\int_0^t v(t)dt} = \frac{\mu_3}{\mu_1}. \tag{22}$$

We define the inequality

$$\mu_3 \geq \mu_2^{3/2} \geq \mu_1^3, \tag{23}$$

which is valid for any inhomogeneous vertically varying medium, and dividing by μ_1 we obtain

$$\frac{\mu_3}{\mu_1} \geq \frac{\mu_2^{3/2}}{\mu_1} = \mu_2 \cdot \frac{\sqrt{\mu_2}}{\mu_1}. \tag{24}$$

Because $\sqrt{\mu_2}/\mu_1 \geq 1$, it is clear from equation 24 that $\mu_3/\mu_1 \geq \mu_2$. This suggests that $v_{\mathrm{rms}}(z)$, obtained by averaging in depth, in equation 22 will always exceed the standard rms velocity $v_{\mathrm{rms}}(t)$, obtained by averaging in time, in equation 21. This observation is highlighted by the estimated values of $v_{k,\mathrm{rms}}$ in Table 1. These overestimated rms velocities in depth are likely to result in a lower estimate of interval velocity compared with the Dix inversion in time. However, the estimated interval velocities using equation 20 are displayed in Table 1 and offer good agreement with the true values.

A COMPARISON WITH CONVENTIONAL VELOCITY ANALYSIS

In the early stages of seismic processing, reflection data are typically rearranged into CMP gathers. Each trace within the CMP gather is assumed to have sampled the same subsurface point. This allows traces to be combined (or stacked) to enhance the arrivals of interest, in this case the primary reflections from the common midpoint. We exploit the fact that such arrivals have an NMO defined as follows:

$$\Delta t_{\mathrm{NMO}} = \sqrt{t_0^2 + \frac{x^2}{v_{\mathrm{rms}}^2}} - t_0. \tag{25}$$

For the appropriate value of t_0 and v_{rms} in equation 25, each trace is shifted upward in time by Δt_{NMO}. Such a procedure removes the effect of offset x and results in the primary reflections being horizon-

Table 1. Estimated velocity and layer thickness results with true values for comparison.

Layer number	Estimated $v_{k,\mathrm{rms}}$ (m/s)	True $v_{k,\mathrm{rms}}$ (m/s)	Estimated D (m)	True D (m)	Estimated v_k (m/s)	True v_k (m/s)
1	1510	1500	210	200	1510	1500
2	1660	1647	200	200	1804	1800
3	1763	1759	200	200	1957	2000

tally aligned in the CMP gather (called NMO correction). After this correction is performed, the traces within each CMP gather are stacked. This results in a single trace recorded at zero-offset above the common midpoint. The aligned primary reflections sum constructively. Other wave types sum destructively and are thus suppressed. For comparison with interferometric velocity analysis, we perform an NMO correction on the CMP gathers of the multilayered model (Figure 7).

Using the complete array of sources and receivers, we group the seismic data into their respective CMP gathers. Figure 12a and d displays CMP gathers 1500 and 2000, respectively. Here, we have applied a time-squared gain and have retained the full wavefield (including multiples). Figure 12b and e shows the corresponding velocity spectra with time-velocity picks. It is not clear which arrivals are primaries and hence which should be picked for NMO correction. In this instance, the multiples are incorrectly handled by the semblance computation, as they are essentially treated as primary arrivals. The events picked allow for an adequate NMO correction in Figure 12c and f. The majority of arrivals appear nicely flattened; however, as is the objective in velocity analysis, we wish for multiple arrivals to stack out and not reinforce. In interferometric velocity analysis, we obtain isolated peaks (in previous figures) because we treat multiples correctly.

DISCUSSION

In the preceding sections, we have shown that interferometric velocity analysis can be used to constrain the interval velocity and layer thickness of a layered acoustic model. There are several advantages and disadvantages of such a method. We begin with the limitations.

First, as with any layer-stripping approach, any error that occurs near the beginning of the process will propagate throughout. We aim to reduce these errors by using multiples to constrain the rms velocity and thickness of each layer. However, there is a trade-off between considering a high number of multiple events and the amount of computation required to calculate traveltime curves. A similar effect occurs when the number of layers or sources are increased. Despite these remarks, the computation time for a four-layer model and 80 sources is approximately 15 minutes. When many more than four layers are considered, however, the method may become overly complex due to the number of orders of multiply reflected waves to be considered. Therefore, we remark that interferometric velocity analysis works well to characterize a small number of horizontal layers beneath a receiver array.

Another drawback is that we have to know what range of velocities and layer thicknesses to use in the semblance computation. However, this same drawback is encountered during the generation of a standard velocity spectrum (Figure 12b and e), where a suitable range of velocities and vertical two-way traveltimes must be defined. We use realistic parameters of D and v that span a broad range of values. However, some prior knowledge from well logs or from other means may prove beneficial.

Similar to NMO analysis, here we assume a sequence of horizontal layers. In its current form, interferometric velocity analysis breaks down in the presence of dip. For an inclined interface, the traveltime of the primary arrival is dependent on the perpendicular depth from the source to reflector and on the dip angle of the interface. If the shot position is moved laterally, the depth point of the primary arrival shifts accordingly. Therefore, in a method such as ours that relies on the traveltime differences between numerous shots, to invert for a single depth point would be meaningless. Such a procedure, although feasible, becomes highly complicated when multiples are considered, and a dip moveout analysis would achieve the required objective.

Despite these disadvantages, interferometric velocity analysis has several benefits. In our interferometric examples, we correctly use multiple energy to constrain the velocity and layer-thickness estimate. As demonstrated in the previous section, this contrasts with conventional velocity analysis, where multiple arrivals are usually

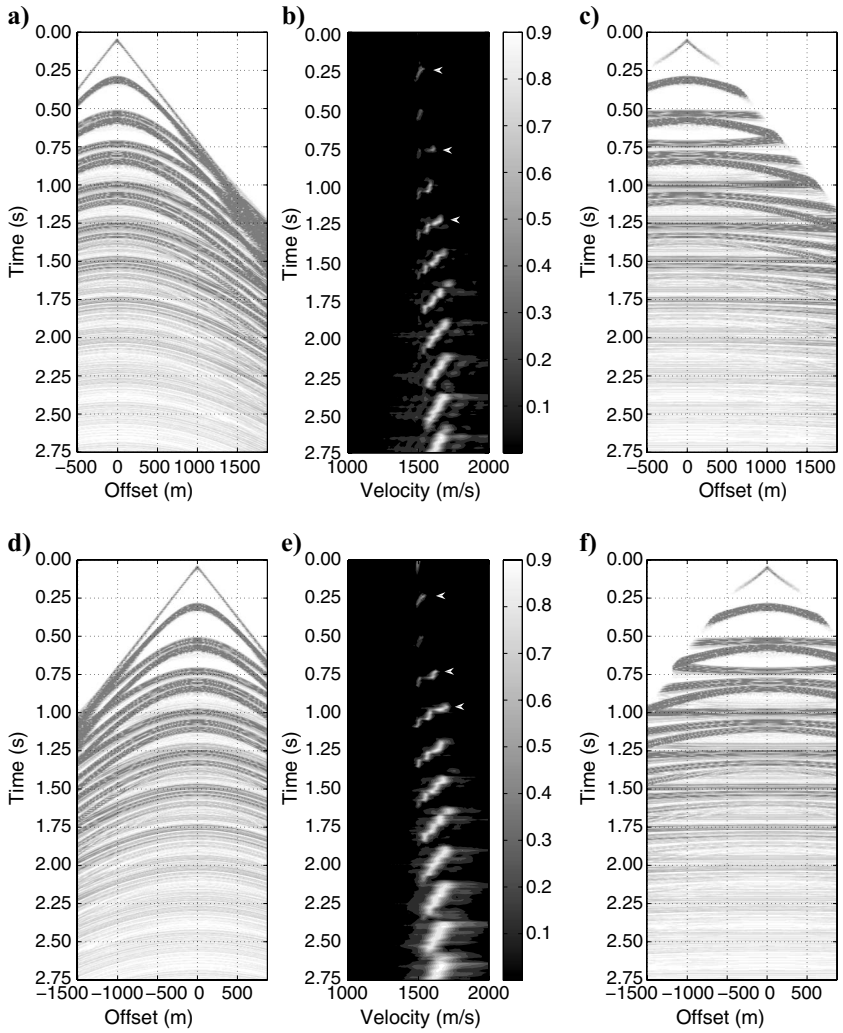

Figure 12. NMO correction performed on two CMP gathers from Figure 7. (a) CMP 1500. (b) Velocity spectrum for CMP 1500. (c) NMO-corrected CMP 1500. (d) CMP 2000. (e) Velocity spectrum for CMP 2000. (f) NMO-corrected CMP 2000. In (b) and (e), white arrowheads show where time-velocity picks were made.

ignored and only primary arrivals are picked. Moreover in some cases, such as the NMO-corrected gathers in Figure 12c and f, conventional velocity analysis treats multiples as primaries, causing the multiple arrivals to align. On the other hand, interferometric velocity analysis treats multiples differently from primaries — all are considered with their correct ray geometries. Although in the multilayered case we remove the direct arrival from each common shot gather, the fact that we consider multiply reflected wavefields means that interferometric velocity analysis is closer to a full wavefield-based technique.

Interferometric velocity analysis is applicable to only a single receiver pair at a time. This has two advantages. First, in seismic surveys in which a large number of receivers are deployed, the technique allows for velocity and layer-thickness estimation between fixed receiver pairs. This allows for a high spatial frequency of velocity and layer-thickness estimates to be computed because there are usually a higher density of receivers than sources. Second, and perhaps more important, in areas where sparse source and receiver coverage exists (for example, in areas of complex terrain or where ocean-bottom receivers are deployed), CMP methods may not be applicable. In these settings, interferometric velocity analysis provides a direct alternative to conventional velocity estimation. In fact, as we have shown, we achieve high-coherence estimates when only 80 sources are considered. However, we should bear in mind that these values may not be the most accurate (using all sources appears better in Figure 10); a degree of interpretation is therefore required. However, the method is ideally suited to applications where source coverage is limited. Furthermore, because these sources may be positioned far from the receiver pair, the method is compatible with long-offset seismic reflection data. By source-receiver reciprocity, all of the above remains true if sources and receivers are interchanged.

So far we have discussed interferometric velocity analysis with respect to crosscorrelation- and deconvolution-type interferometry because the required source-receiver geometries can be approximated using conventional marine data acquisition. However, interferometry can be performed by crossconvolution using an equation not dissimilar to equation 2:

$$\hat{G}(\mathbf{x}_1,\mathbf{x}_2,\omega) \approx \oint_S \frac{2}{\rho c}\hat{G}(\mathbf{x}_1,\mathbf{x},\omega)\hat{G}(\mathbf{x}_2,\mathbf{x},\omega)d^2\mathbf{x}. \tag{26}$$

A third interferometric gather, the convolution gather, can therefore be defined similarly to the other gathers described. In crossconvolutional interferometry, we require a slight modification to the usual geometry of sources and receivers in Figure 1: it is necessary that one of the pair of receivers be positioned outside the source boundary. For example, in the single layer over a half-space model as shown in Figure 2, we can fulfill this requirement by considering receivers 1 and 151 and only the portion of the source boundary between 170 and 400. In that case, we can imagine that if this portion had been complemented with sources in two vertical lines below sources 170 and 400, plus along a horizontal section at depth, receiver 1 would be outside this boundary. Figure 13a shows the corresponding convolution gather using only the surface sources. Figure 13b displays the Green's function estimate, and Figure 13c shows the true Green's function. In Figure 13a, the physical energy (i.e., the stationary-phase region) is located between source numbers 170 and 240. Outside this region, the remaining energy can be considered largely nonphysical. In contrast to crosscorrelation inteferometry, now any significant energy occurs at the traveltime summations

$$\sigma\mathbf{t} = \frac{\sqrt{x_j^2 + (2b_jD_1 \pm z_s \pm z_j)^2}}{v_1} + \frac{\sqrt{x_i^2 + (2b_iD_1 \pm z_s \pm z_i)^2}}{v_1} \tag{27}$$

between waves recorded at both receivers rather than the traveltime difference. We perform interferometric velocity analysis as before, where semblance is defined by equations 8–10, but now we use the traveltime summation equation 27. Figure 14a shows the semblance computed using energy up to the sixth-order multiple ($b = 7$) using sources 170–240, located in the stationary phase region of the convolution gather. We obtain a velocity and layer-thickness pair that lies close to the true values of 1500 m/s and 150 m. Figure 14b shows the semblance computed using energy up to the sixth-order multiple ($b = 7$) using sources 240–400, located in the nonstationary region of the convolution gather. Although our estimate of velocity remains good, the layer-thickness estimate is smeared along the vertical axis. As we now deal with the traveltime summations in equation 27, the convolutions between reflected wavefields (excited far from the receiver pair) appears very close together (e.g., see the nonstationary region between sources 240–400 in Figure 13a). This contrasts with the correlation gather, where the crosscorrelation of reflected wavefields appears farther apart than the respective wavefields at the stationary-phase point (e.g., see the nonstationary region in Figure 4d). The smearing in Figure 14b may be a direct consequence of the converging wavefields in Figure 13a. We suggest that if sources are predominantly located in the stationary-phase position, convolution interferometric velocity analysis may work sufficiently well. On the other hand, if sources are positioned in the nonstationary regions, as is the usual case in long-

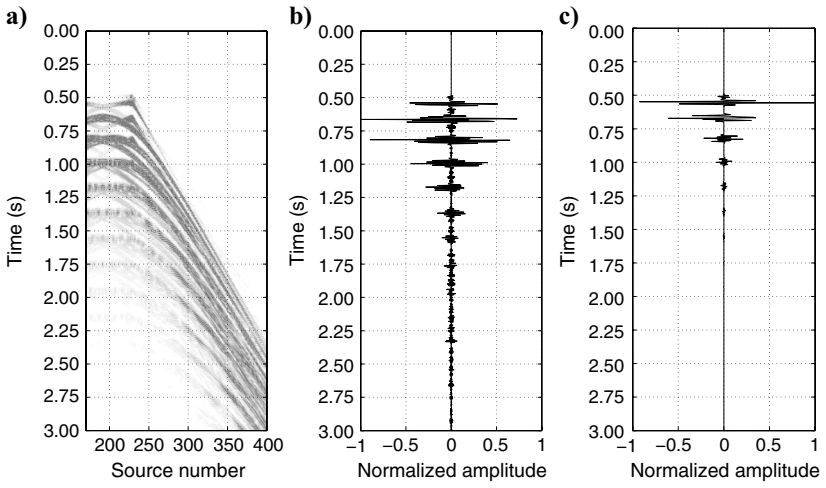

Figure 13. Interferometric estimates and true Green's function for the single layer over half-space model in Figure 2. (a) Convolution gather for receivers 1 and 151 showing arrivals between 0 s and 3 s. (b) Green's function estimate after summation over source position in (a). (c) True Green's function.

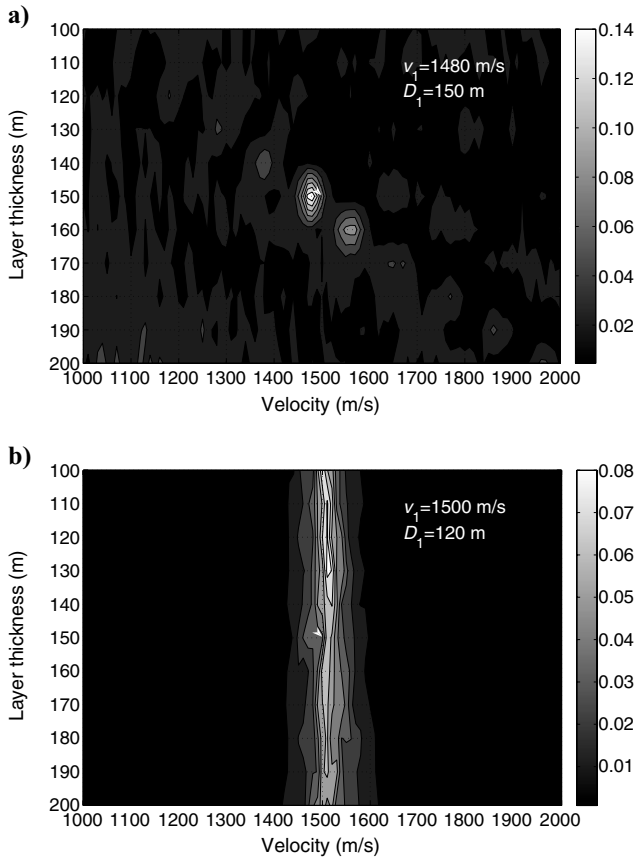

Figure 14. (a) Spectrum showing v_1 against D_1 calculated using source numbers 170–240, located in the stationary-phase region. The velocity v_1 spans from 1000 to 2000 m/s and increments every 10 m/s. The layer thickness D_1 spans from 100 to 200 m and increments every 10 m. We use a time window of 10 ms. (b) As for (a) but computed for source numbers 240–400, located in the nonstationary region.

offset seismic surveys, we suggest that correlation interferometric velocity analysis may provide the better option.

Finally, a significant theoretical contribution of this paper is to show that a great deal of information lies within — and hence, can in principle be extracted from — the nonphysical energy contributions to interferometric wavefields. This corroborates the results of previous studies, which have used nonphysical wavefields to derive refraction velocities (Mikesell et al., 2009) and new optical theorems (Halliday and Curtis, 2009a) and shows that rms velocities are also recoverable from this energy.

CONCLUSIONS

In seismic interferometry, the correlation gather is typically summed over the source position to produce the interreceiver Green's function. The resulting summation removes a significant amount of nonstationary energy (termed nonphysical energy in seismic interferometry) through destructive interference. However, this nonphysical energy provides valuable information about the physical rock properties of the subsurface. We describe a method that uses both the physical and nonphysical energy to obtain this information from the correlation gathers, called interferometric velocity analysis. The method constrains the rms velocity and layer thickness of a horizontally layered synthetic acoustic model, which allows us to estimate interval velocity.

We use the multiply reflected wavefield (both free-surface multiples and interbed multiples) to further constrain rms velocity and layer-thickness estimates. Traditionally, these arrivals are handled incorrectly in, or even suppressed prior to the onset of, velocity analysis. We find that by including the multiply reflected wavefield, we achieve better constrained rms velocity and layer-thickness estimates. We show that by using sources positioned near the endpoints of the source boundary, which contribute mainly to nonphysical energy, we achieve a better-defined estimate of rms velocity and layer thickness. The method may be ideally suited to both short- and long-offset reflection data.

Unlike conventional CMP techniques, which require a large array of both sources and receivers, we require only two receivers and a small array of sources (or, by reciprocity, two sources and an array of receivers). This has implications in exploration seismology, for example in land data or ocean-bottom seismics, where sparse source and receiver coverage may limit the application of CMP analysis. In these situations, our method may provide a direct alternative to conventional methods of velocity estimation. We do not expect our method to replace conventional CMP analysis; however, it may be used in conjunction with it as an additional processing tool.

ACKNOWLEDGMENTS

We thank WesternGeco for permission to publish this work. We acknowledge support from the Scottish Funding Council for the ECOSSE Joint Research Institute with the Heriot-Watt University, which is a part of the Edinburgh Research Partnership in Engineering and Mathematics. We thank Deyan Draganov, Dylan Mikesell, Kurang Mehta, and an anonymous reviewer for their valuable comments, which improved the manuscript.

APPENDIX A

EXTENSION OF THE SHIFTED HYPERBOLA EQUATION TO ACCOUNT FOR MULTIPLE RAYPATHS WITHIN EACH LAYER

Taner and Koehler (1969) showed that for a horizontally layered earth, the square of the traveltime t^2 can be expressed as a power series with respect to the horizontal distance x^2:

$$t^2 = c_1 + c_2x^2 + c_3x^4 + c_4x^6 + \cdots, \qquad \text{(A-1)}$$

where the coefficients $c_1,c_2,c_3,\ldots$ are constants dependent on the layer thickness and seismic velocity of subsurface strata. When the maximum offset is small compared with the depth of target, equation A-1 is truncated to the first two terms, with c_1 and c_2 defined as

$$c_1 = \left(\sum_{k=1}^{M} t_k\right)^2, \qquad \text{(A-2)}$$

$$c_2 = \frac{\sum_{k=1}^{M} t_k}{\sum_{k=1}^{M} t_k v_k^2} \equiv \frac{1}{v_{\text{rms}}^2}, \tag{A-3}$$

where t_k and v_k are the zero-offset two-way traveltime and interval velocity in the kth layer, respectively, and v_{rms} is the rms velocity.

Through close inspection of the acoustic model in Figure 7, it is clear that the maximum offset, for example from source 1 to receiver 301, greatly exceeds the depth to the third layer. Thus, equation A-1 will become inaccurate at these far offsets.

One way to obtain higher accuracy at far offset is to include the fourth-order term in x in equation A-1 (Yilmaz, 2001). However, the term c_3, as well as coefficients c_4 and c_5, becomes increasingly complex and difficult to compute. To overcome this difficulty, Castle (1994) showed that the traveltime equation A-1, exact to the fourth order, can be expressed as a time-shifted hyperbola of the following form:

$$t = t_0\left(1 - \frac{1}{S}\right) + \sqrt{\left(\frac{t_0}{S}\right)^2 + \frac{x^2}{S v_{\text{rms}}^2}} \tag{A-4}$$

where t_0 is the zero-offset two-way traveltime:

$$t_0 = \sum_{k=1}^{M} t_k = 2\sum_{k=1}^{M} \frac{D_k}{v_k}. \tag{A-5}$$

Here, D_k is the layer thickness of the kth layer. Before defining S, we let

$$\mu_j = \frac{1}{t_0}\sum_{k=1}^{M} v_k^j t_k. \tag{A-6}$$

The constant S is equal to

$$S = \frac{\mu_4}{\mu_2^2}. \tag{A-7}$$

Note that

$$\mu_2 = v_{\text{rms}}^2. \tag{A-8}$$

When S takes the value of 1, the shifted hyperbola traveltime in equation A-4 assumes the traveltime in equation A-1 up to the second order.

We wish to extend the traveltime in equation A-4 to account for multiple raypaths within each layer. To achieve this objective, we simply replace the two-way traveltime t_0 in equation A-5 by an equation of the form,

$$t_{0_{\text{mult}}} = \sum_{k=1}^{M} t_k = 2\sum_{k=1}^{M} \frac{b_{k,j} D_k}{v_k}, \tag{A-9}$$

where $b_{k,j}$ is the number of bounce points in the kth layer to the jth receiver. Hence, equations A-6 and A-7 change accordingly. Substituting $t_{0_{\text{mult}}}$ and the appropriate form of equation A-6 and A-7 into the time-shifted hyperbola traveltime, equation A-4 is expressed as

$$t = t_{0_{\text{mult}}}\left(1 - \frac{1}{S}\right) + \sqrt{\left(\frac{t_{0_{\text{mult}}}}{S}\right)^2 + \frac{x^2}{S v_{\text{rms}}^2}}. \tag{A-10}$$

It is important to note that for the uppermost layer (i.e., when $k = 1$ in equation A-9), any term involving the layer thickness D_1 suggests that the traveltime is computed through the complete layer. This is consistent only when both sources and receivers are positioned at the surface of the earth. In fact, the acquisition geometry of Figure 7 illustrates that sources and receivers are positioned at depth beneath the free surface. Therefore, when we compute the traveltime t of a ray passing through layer 1, we must replace $b_{k,j}D_1$ in equation A-9 by the expression $(D_1 + (z_s - z_i) + (b_{k,j} - 1)\cdot D_1)$ where z_s and z_i are the depth of the source and receiver, respectively. For $k \geq 2$, the term $b_{k,j}D_k$ is sufficient.

REFERENCES

Bakulin, A., and R. Calvert, 2006, The virtual source method: Theory and case study: Geophysics, **71**, no. 4, SI139–SI150, doi: 10.1190/1.2216190.

Brekhovskikh, L. M., 1960, Waves in layered media: Academic Press.

Campillo, M., and A. Paul, 2003, Long-range correlations in the diffuse seismic coda: Science, **299**, no. 5606, 547–549, doi: 10.1126/science.1078551.

Castle, R. J., 1994, A theory of normal moveout: Geophysics, **59**, 983–999, doi: 10.1190/1.1443658.

Clayton, R. W., and R. A. Wiggins, 1976, Source shape estimation and deconvolution of teleseismic body-waves: Geophysical Journal of the Royal Astronomical Society, **47**, 151–177.

Curtis, A., P. Gerstoft, H. Sato, R. Snieder, and K. Wapenaar, 2006, Seismic interferometry — Turning noise into signal: The Leading Edge, **25**, 1082–1092, doi: 10.1190/1.2349814.

Curtis, A., and D. Halliday, 2010, Directional balancing for seismic and general wavefield interferometry: Geophysics, **75**, no. 1, SA1–SA14, doi: 10.1190/1.3298736.

Curtis, A., H. Nicolson, D. Halliday, J. Trampert, and B. Baptie, 2009, Virtual seismometers in the subsurface of the earth from seismic interferometry: Nature Geoscience, **2**, no. 10, 700–704, doi: 10.1038/ngeo615.

Diebold, J. B., and P. L. Stoffa, 1981, The traveltime equation, tau-p mapping, and inversion of common midpoint data: Geophysics, **46**, 238–254, doi: 10.1190/1.1441196.

Dix, C. H., 1955, Seismic velocities from surface measurements: Geophysics, **20**, 68–86, doi: 10.1190/1.1438126.

Douma, H., and R. Snieder, 2006, Correcting for bias due to noise in coda wave interferometry: Geophysical Journal International, **164**, no. 1, 99–108, doi: 10.1111/j.1365-246X.2005.02807.x.

González-Serrano, A., and J. F. Claerbout, 1984, Wave-equation velocity analysis: Geophysics, **49**, 1432–1456, doi: 10.1190/1.1441772.

Halliday, D., and A. Curtis, 2008, Seismic interferometry, surface waves and source distribution: Geophysical Journal International, **175**, no. 3, 1067–1087, doi: 10.1111/j.1365-246X.2008.03918.x.

Halliday, D., and A. Curtis, 2009a, Generalized optical theorem for surface waves and layered media: Physical Review E, Statistical, Nonlinear, and Soft Matter Physics, **79**, no. 5, 056603, doi: 10.1103/PhysRevE.79.056603.

Halliday, D., and A. Curtis, 2009b, Seismic interferometry of scattered surface waves in attenuative media: Geophysical Journal International, **178**, no. 1, 419–446, doi: 10.1111/j.1365-246X.2009.04153.x.

Koren, Z., and I. Ravve, 2006, Constrained Dix inversion: Geophysics, **71**, no. 6, R113–R130, doi: 10.1190/1.2348763.

Kumar, P., K. Sain, and H. C. Tewari, 2003, A direct method of estimating depth to a reflector from seismic wide-angle reflection times: Geophysical Journal International, **152**, no. 3, 740–748, doi: 10.1046/j.1365-246X.2003.01891.x.

Mehta, K., A. Bakulin, J. Sheiman, R. Calvert, and R. Snieder, 2007, Improving the virtual source method by wavefield separation: Geophysics, **72**, no. 4, V79–V86, doi: 10.1190/1.2733020.

Mehta, K., R. Snieder, R. Calvert, and J. Sheiman, 2008, Acquisition geometry requirements for generating virtual-source data: The Leading Edge, **27**, 620–629, doi: 10.1190/1.2919580.

Mikesell, D., K. van Wijk, A. Calvert, and M. Haney, 2009, The virtual refraction: Useful spurious energy in seismic interferometry: Geophysics, **74**, no. 3, A13–A17, doi: 10.1190/1.3095659.

Muijs, R., J. O. A. Robertsson, and K. Holliger, 2007, Prestack depth migration of primary and surface-related multiple reflections: Part I — Imaging: Geophysics, **72**, no. 2, S59–S69, doi: 10.1190/1.2422796.

Neidell, N. S., and M. T. Taner, 1971, Semblance and other coherency measures for multichannel data: Geophysics, **36**, 482–497, doi: 10.1190/1.1440186.

Nowroozi, A. A., 1990, Interpretation of seismic reflection records: Direct calculation of interval velocities and layer thicknesses from travel-times: Pure and Applied Geophysics, **133**, 103–115, doi: 10.1007/BF00876705.

Robertsson, J. O. A., J. O. Blanch, and W. W. Symes, 1994, Viscoelastic finite-difference modeling: Geophysics, **59**, 1444–1456, doi: 10.1190/1.1443701.

Sabra, K. G., P. Roux, and W. A. Kuperman, 2005, Arrival-time structure of the time-averaged ambient noise cross-correlation function in an oceanic waveguide: The Journal of the Acoustical Society of America, **117**, no. 1, 164–174, doi: 10.1121/1.1835507.

Sain, K., and K. L. Kaila, 1996, Direct calculation of interval velocities and layer thicknesses from seismic wide-angle reflection times: Geophysical Journal International, **125**, no. 1, 30–38, doi: 10.1111/j.1365-246X.1996.tb06532.x.

Schultz, P. S., 1982, A method for direct estimation of interval velocities: Geophysics, **47**, 1657–1671, doi: 10.1190/1.1441315.

Schuster, G. T., J. Yu, J. Sheng, and J. Rickett, 2004, Interferometric/daylight seismic imaging: Geophysical Journal International, **157**, no. 2, 838–852, doi: 10.1111/j.1365-246X.2004.02251.x.

Slob, E., D. Draganov, and K. Wapenaar, 2007, Interferometric electromagnetic Green's functions representations using propagation invariants: Geophysical Journal International, **169**, no. 1, 60–80, doi: 10.1111/j.1365-246X.2006.03296.x.

Slob, E., and K. Wapenaar, 2007, Electromagnetic Green's functions retrieval by cross-correlation and cross-convolution in media with losses: Geophysical Research Letters, **34**, no. 5, L05307, doi: 10.1029/2006GL029097.

Snieder, R., 2004, Extracting the Green's function from the correlation of coda waves: A derivation based on stationary phase: Physical Review E, Statistical, Nonlinear, and Soft Matter Physics, **69**, no. 4, 046610, doi: 10.1103/PhysRevE.69.046610.

Snieder, R., M. Miyazawa, E. Slob, I. Vasconcelos, and K. Wapenaar, 2009, A comparison of strategies for seismic interferometry: Surveys in Geophysics, **30**, no. 4–5, 503–523, , doi: 10.1007/s10712-009-9069-z.

Snieder, R., J. Sheiman, and R. Calvert, 2006a, Equivalence of the virtual-source method and wave-field deconvolution in seismic interferometry: Physical Review E, Statistical, Nonlinear, and Soft Matter Physics, **73**, no. 6, 066620, doi: 10.1103/PhysRevE.73.066620.

Snieder, R., K. van Wijk, M. Haney, and R. Calvert, 2008, Cancellation of spurious arrivals in Green's function extraction and the generalized optical theorem: Physical Review E, Statistical, Nonlinear, and Soft Matter Physics, **78**, no. 3, 036606, doi: 10.1103/PhysRevE.78.036606.

Snieder, R., K. Wapenaar, and K. Larner, 2006b, Spurious multiples in seismic interferometry of primaries: Geophysics, **71**, no. 4, SI111–SI124, doi: 10.1190/1.2211507.

Taner, M. T., and F. Koehler, 1969, Velocity spectra-digital computer derivation applications of velocity functions: Geophysics, **34**, 859–881, doi: 10.1190/1.1440058.

van der Neut, J., and A. Bakulin, 2009, Estimating and correcting the amplitude radiation pattern of a virtual source: Geophysics, **74**, no. 2, SI27–SI36, doi: 10.1190/1.3073003.

van Manen, D.-J., A. Curtis, and J. O. A. Robertsson, 2006, Interferometric modeling of wave propagation in inhomogeneous elastic media using time reversal and reciprocity: Geophysics, **71**, no. 4, SI47–SI60, doi: 10.1190/1.2213218.

van Manen, D.-J., J. O. A. Robertsson, and A. Curtis, 2005, Modeling of wave propagation in inhomogeneous media: Physical Review Letters, **94**, no. 16, 164301, doi: 10.1103/PhysRevLett.94.164301.

Vasconcelos, I., and R. Snieder, 2008a, Interferometry by deconvolution: Part 1 — Theory for acoustic waves and numerical examples: Geophysics, **73**, no. 3, S115–S128, doi: 10.1190/1.2904554.

Vasconcelos, I., and R. Snieder, 2008b, Interferometry by deconvolution: Part 2 — Theory for elastic waves and application to drill-bit seismic imaging: Geophysics, **73**, no. 3, S129–S141, doi: 10.1190/1.2904985.

Wapenaar, K., 2004, Retrieving the elastodynamic Green's function of an arbitrary inhomogeneous medium by cross correlation: Physical Review Letters, **93**, no. 25, 254301, doi: 10.1103/PhysRevLett.93.254301.

Wapenaar, K., and J. Fokkema, 2006, Green's function representations for seismic interferometry: Geophysics, **71**, no. 4, SI33–SI46, doi: 10.1190/1.2213955.

Wapenaar, K., J. van der Neut, and E. Ruigrok, 2008, Passive seismic interferometry by multidimensional deconvolution: Geophysics, **73**, no. 6, A51–A56, doi: 10.1190/1.2976118.

Yilmaz, Ö., 2001, Seismic data analysis: SEG.